ORIGINAL PAPER

Interface reaction of high-strength low-alloy steel with Al–43.4Zn–1.6Si (wt.%) metallic coating

Wang-jun Peng[1,2,3] · Guang-xin Wu[1,2,3] · Yi Cheng[1,2,3] · Jie-yu Zhang[1,2,3]

Abstract

The microstructure, elemental distribution, phase composition, and thickness of intermetallic layers between high-strength low-alloy steel (H420)/mild carbon steel (DC51) and Al–43.4Zn–1.6Si (wt.%) (galvalume, GL) alloy were comparatively investigated. The experimental results reveal that the interfacial reaction layer was composed of Fe_2Al_5, Fe_4Al_{13}, and Al_8Fe_2Si intermetallic compounds. Moreover, the growth curves of the Fe_2Al_5 and Fe_4Al_{13} intermetallic layers fit the parabolic law well, and the total thickness of the intermetallic layers of H420 + GL was almost the same as that of DC51 + GL. However, the thickness of the Fe_2Al_5 layer in H420 + GL was thinner than that in DC51 + GL. In addition, first-principle calculations were performed to explore the effect of Mn on the growth of the Fe_2Al_5 intermetallic phase, and the results indicate that Mn substitution in Fe_2Al_5 removes electronic charge from the Al atoms, thus decreasing the thickness of the Fe_2Al_5 interface layer.

Keywords High-strength low-alloy steel · Mild carbon steel · Al–43.4Zn–1.6Si (wt.%) alloy · Interface reaction

1 Introduction

High-strength low-alloy (HSLA) steel is used in many fields such as energy, transportation, construction, and engineering machinery, especially in the construction industry. Every year, a large amount of HSLA steel is consumed because of the rapid development of China's economy. HSLA steels are widely used because of their low price, excellent performance, and easy recycling. Research into HSLA steels has focused on obtaining materials with improved strength, lamellar tearing resistance, resistance to thermal shock, weather resistance, and weldability.

HSLA steels must be corrosion protected before use in harsh conditions, and many methods have been tested to prolong the lifespan of steel. Metallic coating is an effective method to prevent steel corrosion under severe atmospheric conditions. The Al–43.4Zn–1.6Si (wt.%) alloy coating is one metallic coating used in BlueScope steel and has distinct advantages, providing a physical barrier between the steel substrate and the corrosive environment [1].

To date, many studies of the morphology of Fe substrates and the growth kinetics of Fe–Al intermetallic layers on aluminum coatings have been reported. It is well known that the reaction between liquid Al and solid Fe forms a Fe–Al alloy layer consisting of Fe_2Al_5 and $FeAl_3$ phases [2–5]. In addition, investigation of Al–Si coatings has also been proposed. Nazari and Shabestari [6] reported the morphology and growth kinetics of intermetallic compounds formed at the interface of H13 tool steel and A380 molten aluminum; they found that three intermetallic layers formed through the liquid–solid reaction during the immersion of steel samples into liquid aluminum at 680 °C from 2 min to 2.5 h, and these intermetallic compounds are τ_5 (Al_8Fe_2Si), τ_6 (Al_5FeSi), and $Al_{12}Fe_5Si$. Cheng and Wang [7] investigated the phase transformation in a Si-modified aluminide coating on mild steel using the electron backscatter diffraction (EBSD) method and found that the

✉ Guang-xin Wu
gxwu@t.shu.edu.cn

1 State Key Laboratory of Advanced Special Steel, Shanghai University, Shanghai 200072, China

2 Shanghai Key Laboratory of Advanced Ferrometallurgy, Shanghai University, Shanghai 200072, China

3 School of Materials Science and Engineering, Shanghai University, Shanghai 200072, China

dominant phases in the intermetallic layer were τ_5, FeAl$_3$ and Fe$_2$Al$_5$ with dispersive τ_1 (Al$_2$Fe$_3$Si$_3$). Springer et al. [8] investigated the effect of Si addition on Fe diffusion in the Fe$_2$Al$_5$ phase and found that the growth rate of the intermetallic phases increased with increasing Si content. Jiang et al. [9] investigated the effects of zinc coating on the interfacial microstructures of the aluminum/steel bimetallic composites prepared by a solid–liquid diffusion method and found that the reaction layer at the interface between the aluminum and the steel was mainly composed of τ_6, α-Al, α-Al +η-Zn eutectoid, η-Zn, and eutectic silicon phases. As reported in Ref. [10], aluminum/iron bimetallic composites have been successfully fabricated using ZL114A alloy and gray cast iron by the hot-dip aluminizing method. These composites have a relatively uniform and compact reaction layer mainly consisting of Fe$_2$Al$_5$, τ_{10} (Al$_9$Fe$_4$Si$_3$), FeAl$_3$, τ_5, and τ_6 intermetallic compounds between the aluminum and iron.

In addition, numerous papers concerning hot-dip Al–Zn coatings have been published. Phelan et al. [11] reported the formation of intermetallic phases on steel substrates immersed in Al–43.4Zn–1.6Si (wt.%) baths, and the result showed that the reaction layer formed on the samples dipped in a 1.5 wt.% silicon bath comprised two intermetallic species: α-AlFeSi and Fe$_2$Al$_5$. In contrast, in the 1.3 wt.% bath, there were three clearly identifiable intermetallic species: α-AlFeSi, FeAl$_3$, and Fe$_2$Al$_5$. Peng et al. [12] investigated the effect of Cu and Si on hot-dip galvalume coatings, revealing that Cu can effectively control the Fe–Al reactivity because of its synergistic effect with Si; that is, the addition of Cu resulted in Si enrichment in the reaction region during the hot-dipping, which promoted the formation of the τ_5 phase and hindered the growth of the Fe$_2$Al$_5$ phase. Selverian et al. [13] reported the effect of various silicon concentrations on the reaction between iron panels and Al–Zn–Si liquid baths during hot-dipping at 610 °C. They found that the intermetallic layer was the thinnest for a 3 wt.% silicon bath, and the growth was interface reaction controlled in 3 and 5 wt.% silicon baths.

The technological process of treating mild carbon steel by hot-dipping with an Al–43.4Zn–1.6Si (wt.%) metallic coating has received much attention [14]. The effect of Ti addition on the thickness and adhesion of an Al–43.4Zn–1.6Si (wt.%) coating has been predicted by first-principle calculations, and the results indicate that Ti atoms remove electronic charge from the Al atoms, thus forming bonds with neighboring Al atoms, which reduces the growth of the Fe–Al intermetallic layers, enhancing the adhesion of the coating/substrate [15]. Moreover, the microstructure and thickness of Al–43.4Zn–1.6Si–0.2RE (La, Ce) (wt.%) coatings during the hot-dipping of Q235 steel were also investigated [16]. The experimental results reveal that the intermetallic layer was composed of Fe$_2$Al$_5$, FeAl$_3$, and τ_5

phases, and first-principle calculations indicate that La substitution in the Fe$_2$Al$_5$ and FeAl$_3$ phases can remove electronic charge from Al atoms and weaken the formation of Fe–Al compounds.

Internal and external oxidation problems seldom exist in mild carbon steel treated by the hot-dip Al–43.4Zn–1.6Si (wt.%) process. However, leaking points, a thick coating and gray surface, poor adhesion, and other engineering problems are observed after the addition of Mn and Si in high-strength low-alloy steel treated by hot-dipping [17, 18]. The main reason for this is the selective oxidation of Mn and Si on the steel surface [19, 20], that is, non-wetting behavior will be present in high-strength steels when treated by hot-dipping with Zn alloy [21, 22]. The unavoidable presence of O$_2$ and H$_2$O within the controlled H$_2$–N$_2$ atmosphere of an industrial annealing furnace can lead to the appearance of considerable amounts of external MnO or Mn–Si mixed oxides, which disturbs the wetting and reactive wetting in the galvanizing bath and degrades the coating quality [23–25]. Therefore, Mn has a clear influence on the wettability of the steel and will inevitably affect the interfacial reaction. However, information about the effect of Mn in the substrate on the interfacial reaction between the bath and substrate in hot-dip Al–43.4Zn–1.6Si (wt.%) is still insufficient.

In this study, the microstructure, distribution of elements, phase composition and thickness of intermetallic layers between high-strength low-alloy steel (H420)/mild carbon steel (DC51) and Al–43.4Zn–1.6Si (wt.%) alloy were investigated, and we aimed to investigate the effect of the Mn in the Fe substrate on the morphology and growth kinetics of hot-dip Al–Zn coatings.

2 Experimental

2.1 Experimental materials

DC51 and H420 steels with a thickness of 1.0 mm were cut into panels with dimensions of 30 mm × 5 mm. The galvalume alloy (Al–43.4Zn–1.6Si (wt.%), GL) for the experiment was a commercial product manufactured by Zhuzhou Smelter Group (Zhuzhou City, China). The actual elemental compositions of the steel and GL alloy were determined by inductively coupled plasma mass spectrometry (ICP-MS), and the results are given in Table 1.

2.2 Experimental process

Al–43.4Zn–1.6Si (wt.%) alloy was machined into a bulk piece with dimensions of 5 mm × 5 mm × 25 mm, and the steel panels were mechanically polished with 320–1000 mesh SiC papers. Then, the panels were degreased with 10

Steel	C	Si	Mn	P	S	Fe
DC51	0.063	0.110	0.18	0.029	0.013	Balance
H420	0.072	0.076	0.65	0.013	0.015	Balance

wt.% NaOH + NaCO$_3$ solution, the rust was removed with 15 vol.% HCl solution, and the panels were cleaned in distilled water and pure alcohol. Subsequently, the steel panels and GL alloy were placed in quartz tubes (dimensions: $\phi_{Inner} = 8$ mm, $\phi_{outer} = 10$ mm, length = 150 mm) and vacuum sealed. A graphite crucible filled with the quartz tubes was placed in the furnace, and the temperature was increased to 600 °C at a rate of 10 °C/min. Based on the temperature of the zinc pot used in the galvalume industry [26], the furnace temperature was set to 600 °C. The graphite crucible was shaken to fill the quartz tubes with the GL alloy after complete melting, ensuring that the steel panels were in full contact with the melted alloy. Then, the quartz tubes were removed from furnace and water cooled for 60, 180, 300, 420, 540, 720, 960, and 1200 s, respectively. A schematic of the preparation for interfacial reaction samples is given in Fig. 1.

2.3 Experimental analysis equipment

The optical microscope (CMM-33E, Changfang Optical Instrument Co., Ltd., Shanghai, China) was used to characterize the morphology and thickness of the interfacial reaction layers. The sample was mechanically ground with 320–1200 mesh SiC papers and then polished and etched with Keller's etchant (2 mL HF, 3 mL HCl, 5 mL HNO$_3$, and 190 mL distilled water) to reveal the microstructure of
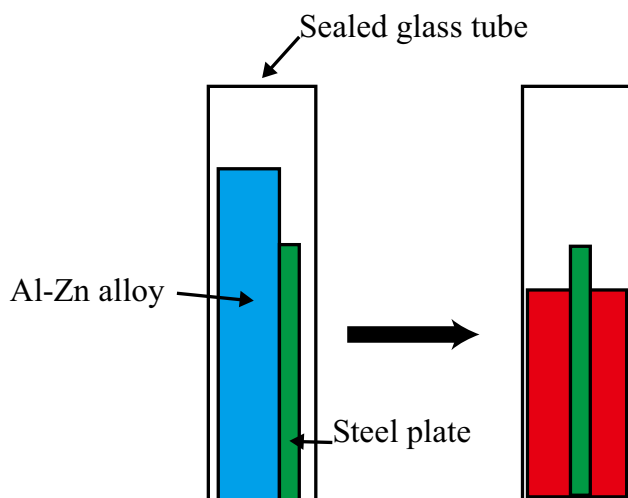

Sealed glass tube

Al-Zn alloy

Steel plate

Fig. 1 Schematic of sample preparation for interfacial reaction investigation

the interfacial reaction layers. The microstructure and elements in the interfacial reaction layer were investigated by scanning electron microscopy (SEM, Apollo300, CamScan, Cambridgeshire, UK) and energy-dispersive X-ray spectroscopy (EDS, X-act One, Oxford,High Wycombe, UK), respectively. X-ray diffractometry (XRD, TTRAX-III, Rigaku, The Woodlands, TX, USA) was used to obtain phase information about the interfacial reaction layer, and Jade 6.0 was used to determine the crystalline phases. The X-ray diffraction patterns were obtained from 20°–100° (2θ) at a rate of 2 (°)/min using monochromatic Cu Kα radiation.

3 Results and discussion

3.1 Microstructure of interfacial reaction layer

Characteristic cross sections of the interfacial reaction layers (DC51 + GL and H420 + GL) at different reaction time are presented in Figs. 2 and 3. As shown in Fig. 2, the interfacial reaction layer comprised two different regions, a dark gray phase close to the steel substrate and a light gray phase near the Al–Zn metallic coating. In addition, the light gray phase became rough with increasing reaction time, which indicates that heat transferred from the substrate to the metallic coating in the solidification process. Solidification is accompanied by the release of latent melting heat, which must be removed by slow conduction along a flat temperature gradient toward the surface layer [27]. A black belt appeared in the interfacial reaction layer of H420 + GL prepared at different reaction time, and the carbon content increased obviously with increasing reaction time. Similar results were reported in Ref. [28].

3.2 Composition of interfacial reaction layer

To analyze the distribution of elements in the interfacial reaction layer, EDS line scans were used, and the result is presented in Fig. 4. The overlayer contained Al and Zn, and the Fe content increased gradually from the overlay to the interfacial reaction layer, whereas the contents of Al and Zn decreased gradually. Si was enriched at the interface between the overlay and interfacial reaction layer; this is denoted as Al–Fe–Si enrichment. This region is beneficial for the adhesion of the Al–Zn coating to the steel panel [16, 29]. It should be noted that signals corresponding to Mn were not obtained in this paper because the Mn content was lower than the detection accuracy of the device.

The compositional distribution of the interfacial reaction layer was analyzed for the interfacial reaction layers of H420 + GL at 180 and 1200 s (Table 2). The average Fe:Al atomic ratios of Spots 1 and 3 near the Al–Zn coating
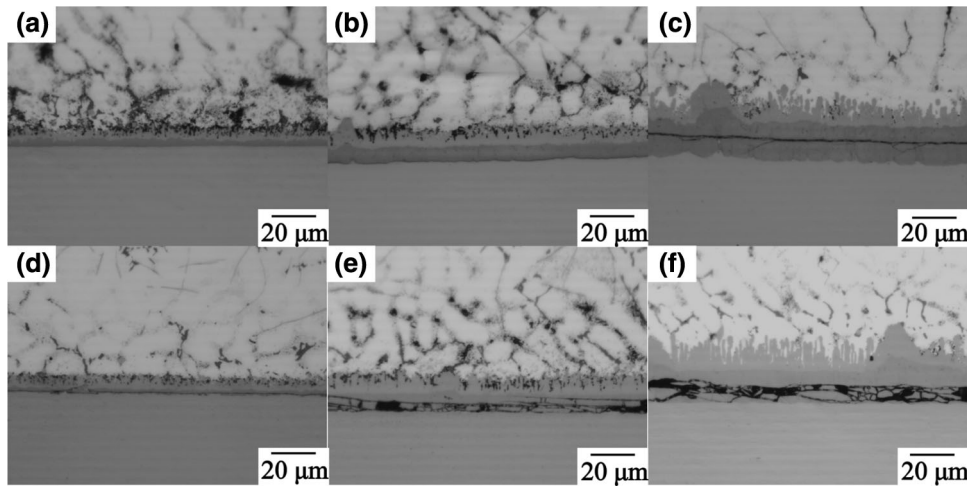
Fig. 2 Cross sections of DC51 + GL (**a**–**c**) and H420 + GL (**d**–**f**) samples at different reaction time. **a**, **d** 60 s; **b**, **e** 300 s; **c**, **f** 1200 s
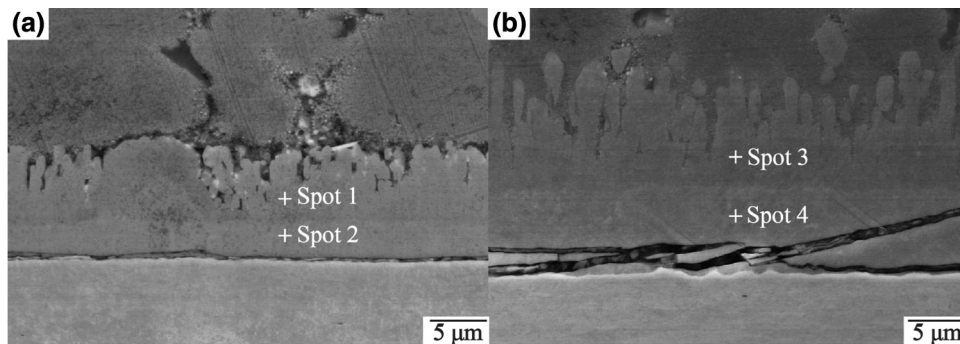

Fig. 3 SEM micrographs of cross sections of H420 + GL samples reacted at 600 °C for 180 s (**a**) and 1200 s (**b**)

are close to the stoichiometry of the Fe_4Al_{13} phase, and the average Fe:Al atomic ratios of Spots 2 and 4 near the steel substrate are close to the stoichiometry of the Fe_2Al_5 phase.

The element distribution of the H420 + GL interfacial reaction layer is consistent with that of DC51 + GL based on the above analysis. Moreover, Al and Fe are the main elements in the interfacial reaction layer with a total content over 90 at.%. Thus, intermetallic compounds were inferred to be Fe–Al-type phases. Other elements, such as zinc or silicon, are present in these compounds as an interstitial or a substitutional solid solution. On the basis of the Al–Zn–Fe phase diagram (Fig. 5) and Fe–Al phase diagram (Fig. 6), which was calculated using Pandat [30] and the PanAl-aluminum alloy thermodynamic database [31], along with the solidification of hot-dip coatings [32], the Fe_2Al_5 and Fe_4Al_{13} phases were present at 600 °C. Therefore, it was confirmed that the interfacial reaction layer consisted of Fe_2Al_5 and Fe_4Al_{13} phases.

In addition, the composition of the black belt ahead of the interfacial reaction layer of the H420 + GL for 1200 s is presented in Fig. 7 and Table 3. The atom percentages of carbon of Spots 4 and 6 were higher than those of Spots 2

and 3 (in Fig. 7), indicating that there is a carbon buildup in these regions. Furthermore, the carbon content increased in the black strip, and this trend became more obvious as the reaction time increased (as shown in Fig. 4).

The coating on the samples was removed by etching (10 vol.% Nital) to allow further interpretation of the carbon buildup phenomenon, and both the substrate morphologies of the raw steel panels and those of the steel panels after heating are shown in Fig. 8. Both substrates are composed of ferrite and pearlite, and the volume fraction of pearlite in H420 steel was higher than that in DC51 steel. Meanwhile, the pearlite in the H420 steel changed from gathered to dispersive after heating, but the pearlite in DC51 steel changed little after heating (as shown in Fig. 8).

The main reason for the different morphologies observed at the raw steel surfaces was that the high-strength low-alloy steel contains more Mn (0.65 wt.%), which promotes the formation of carbides at mid- or high-temperature conditions. The Fe atoms are replaced by Mn atoms and thus an $(Fe, Mn)_3C$ phase is formed by the nucleation of cementite ($(Fe, Mn)_3C$). Mn atoms could also promote the formation of pearlite in steel; thus, the volume
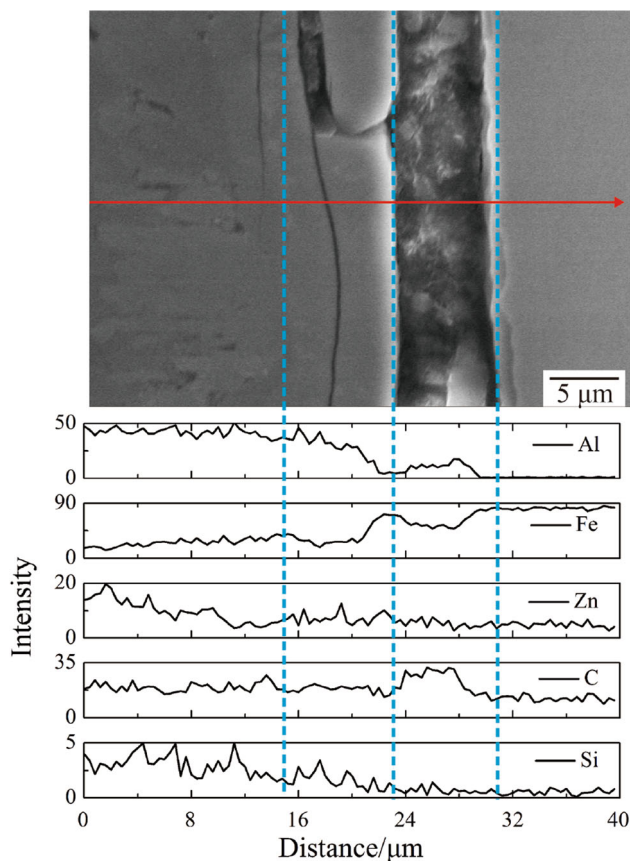
Fig. 4 Concentration distribution of elements in interfacial reaction layers (H420 + GL, 720 s)

Table 2 Composition distribution of interfacial reaction layer (H420 + GL) for 180 s (Spots 1 and 2) and 1200 s (Spots 3 and 4), as defined in Fig. 3 (at.%)

Spot	Al	Si	Fe
Spot 1	72.09	6.06	21.85
Spot 2	70.63	4.91	24.46
Spot 3	73.52	3.82	22.93
Spot 4	70.91	1.91	27.19

Fig. 5 Fe–Al–Zn phase diagram at 600 °C

Fig. 6 Binary Fe–Al phase diagram

of pearlite in the H420 steel was greater than that in the DC51 steel. The reason for the "carbon buildup" ahead of the interface between the H420 steel panel and Al–43.4Zn–1.6Si (wt.%) alloy was that the content of carbide in the H420 steel was greater than that in the DC51 steel, and this could not diffuse through the intermetallic layer during the interfacial reaction. Therefore, the Al atoms drove out the carbon atoms as they diffused toward the interface, resulting in the formation of a carbon buildup ahead of interface. In Ref. [33], the influence of different carbon contents in steel treated with hot-dip Al alloy was reported, and the "carbon buildup" phenomenon was also reported.
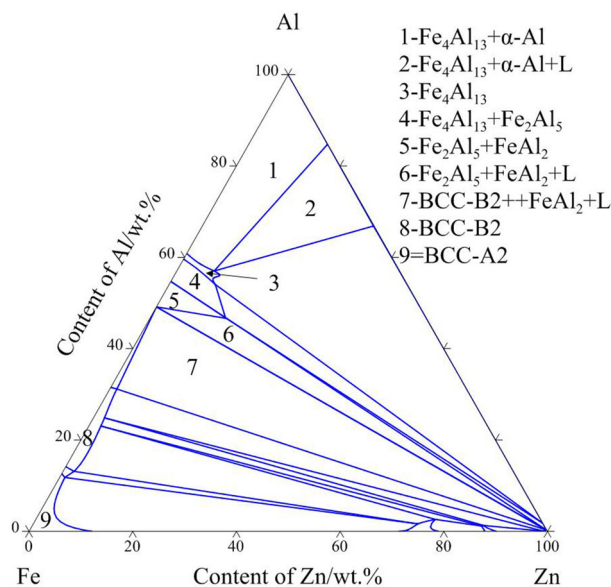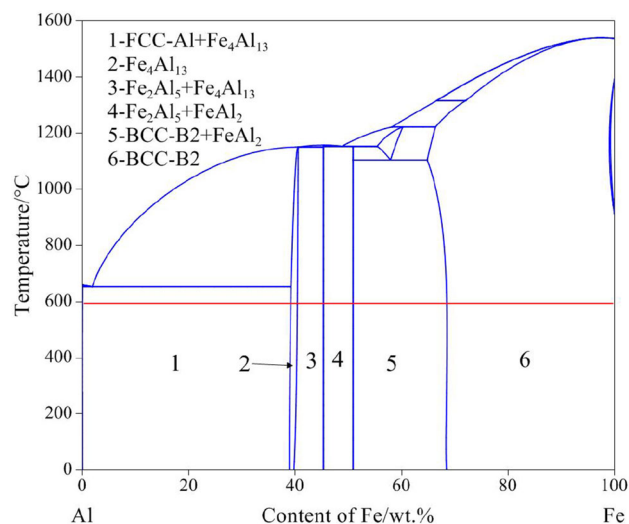
The results show that the carbon diffused in front of the interface and produced the observed "carbon buildup" during the growth from the reaction layer on the steel substrate. On increasing the carbon content of the substrate steel, the growth from the interfacial reaction layer into the steel was impeded by the pearlite phase, that is, the pearlite phase blocked diffusion and restricted the growth of the Fe_2Al_5 layer. The volume fraction of pearlite also increased ahead of the interface, confirming this conclusion [34]. Sasaki et al. [35] also studied the effect of different carbon contents on alloy layer growth during hot-dip aluminum coating, and the results showed that the thickness of the alloy layer decreased as the carbon concentration of the base steel decreased.
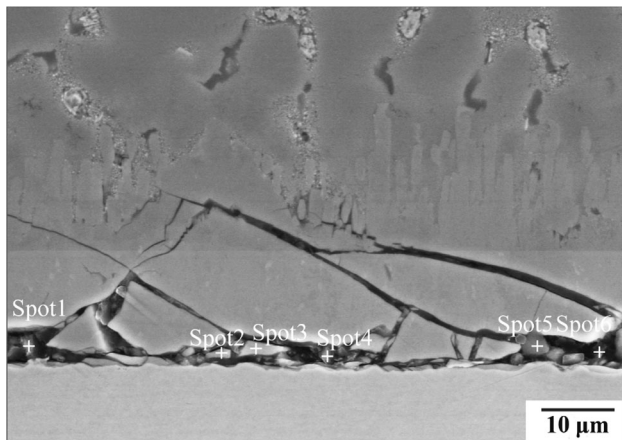
Fig. 7 SEM micrograph of black strip in interface layer (H420 + GL, 1200 s)

Table 3 Compositional distribution of black strip in interface layer (H420 + GL, 1200 s) related to Fig. 7 (at.%)

Spot	C	Al	Si	Fe	Zn
Spot 1	26.97	1.04		70.10	1.25
Spot 2	11.73	0.93		87.34	
Spot 3	12.10	60.50	2.59	22.88	1.93
Spot 4	76.11	5.64		13.12	5.13
Spot 5	21.77	2.22		74.84	1.16
Spot 6	64.67	14.46		12.68	8.20

3.3 Intermetallic phases

To determine the phase composition of the interfacial reaction layer, both samples were grounded layer-by-layer for X-ray diffraction analysis. Figure 9a shows the X-ray diffraction patterns of the dark phase closest to the steel substrate. The diffraction peaks indicate the presence of Fe_2Al_5 and Al phases. Figure 9b shows the X-ray diffraction patterns of the bright gray phase closest to the Al–Zn metallic coating. The diffraction peaks were indexed to Fe_4Al_{13}, Al, Zn, and Al_8Fe_2Si phases, which is consistent with previous results [16]. It should be emphasized that Fe_4Al_{13} (38.9 wt.% Fe) is often reported as $FeAl_3$ (40.7 wt.% Fe) with a probable range of existence of 37 to 41 wt.% Fe [8]. Furthermore, the XRD results revealed that no new intermetallic phase was produced between H420 steel and Al–43.4Zn–1.6Si (wt.%) alloy.

3.4 Thickness of interfacial reaction layer

Image analysis was used to characterize the thickness of interfacial reaction layer as a function of reaction time. At least five images of the interfacial reaction layer were captured for each sample, and the thicknesses of the interfacial reaction layer and Fe_2Al_5 phase were measured. Then, the thickness measurements were converted to average values. A schematic of the thickness of the interfacial reaction layer is shown in Fig. 10 [36].

A change in the total thickness of the interfacial reaction layer with reaction time for the H420 and DC51 steels in three identical parallel experiments is shown in Fig. 11. Referring to the literature results [3, 8], the growth rate of the interfacial reaction layer follows a parabolic law, and the interfacial reaction is controlled by diffusion. The growth dynamics is described by $y = kt^{1/2} + c$, where y is the thickness of the interfacial reaction layer, k is the growth dynamic constant, t is the reaction time, and c is a constant. Thus, the experimental data were fitted using the above growth dynamic equation, revealing that the interfacial reaction layer growth followed a parabolic law in H420 + GL and DC51 + GL (the fitting parameters are listed in Table 4).

The interfacial reaction layer thicknesses of H420 + GL and DC51 + GL increased obviously with increasing reaction time. In particular, the Fe_2Al_5 phase occupied a higher proportion of the total interfacial reaction layer. Although the thickness of the Fe_4Al_{13} phase also increased with the increasing reaction time, the growth rate of the Fe_4Al_{13} phase just increased slowly. These results are consistent with the work of Shahverdi et al. [3], which showed that the Fe_4Al_{13} phase has a monoclinic unit cell, whereas the Fe_2Al_5 phase has an orthorhombic unit cell. Furthermore, thermodynamic calculations have shown that the reaction enthalpy of Fe_4Al_{13} phase is lower in the early stages of the interfacial reaction process compared to that of the Fe_2Al_5 phase [37]. Thus, the Fe_4Al_{13} phase was generated prior to Fe_2Al_5 phase, and the growth rate of the Fe_2Al_5 phase, which forms a thicker layer, was faster in the direction of the c-axis.

Next, the thicknesses of interfacial reaction layers on H420 + GL and DC51 + GL were compared, as shown in Figs. 11 and 12. The results showed that the interfacial reaction layer thicknesses in H420 + GL and DC51 + GL were very similar (Fig. 12a), although the Fe_2Al_5 phase was thinner in H420 + GL (Fig. 12b) than that in DC51 + GL under the same experimental conditions. This indicates that the growth rate of the Fe_2Al_5 phase on high-strength low-alloy steel (H420) was lower than that on mild carbon steel (DC51) because of the high Mn content. The fitting parameters are shown in Table 5.

The samples were analyzed by glow discharge spectroscopy (GDS, Fig. 13) to determine the effect of the Mn in the H420 substrate. It was found that the Mn content decreased gradually from the substrate to the surface of the aluminum–zinc alloy, and the content of Mn is higher in the interfacial reaction layer of H420 + GL steel than that
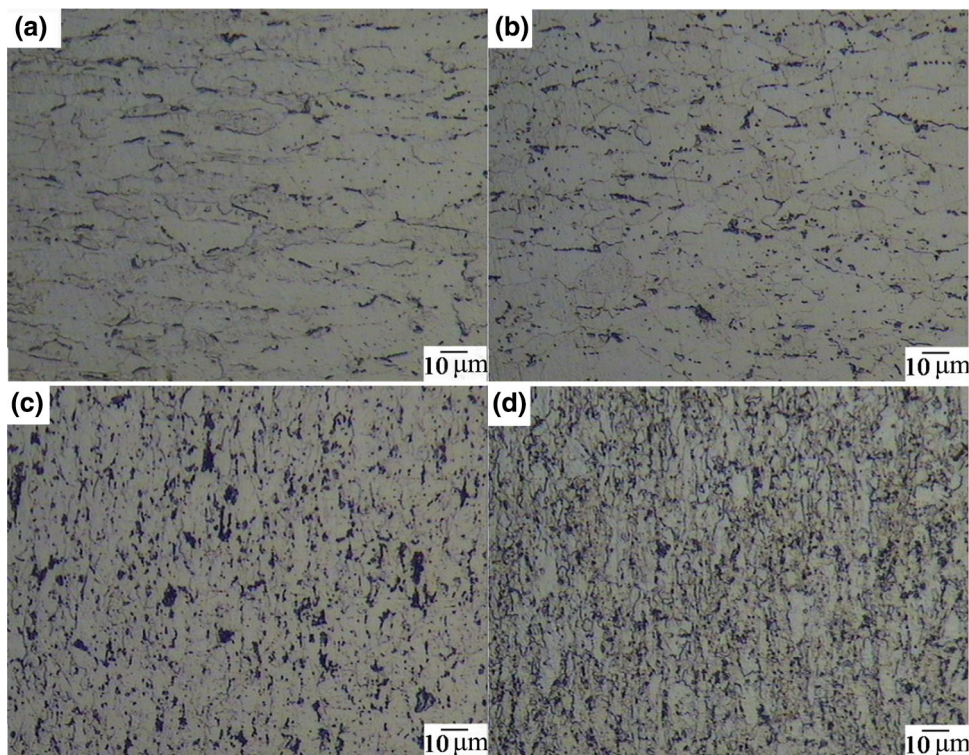
Fig. 8 Surface morphologies of DC51 (**a**, **b**) and H420 (**c**, **d**) steels. **a**, **c** Raw steel panels; **b**, **d** steel panels after dipping in Al–Zn alloy (1200 s)
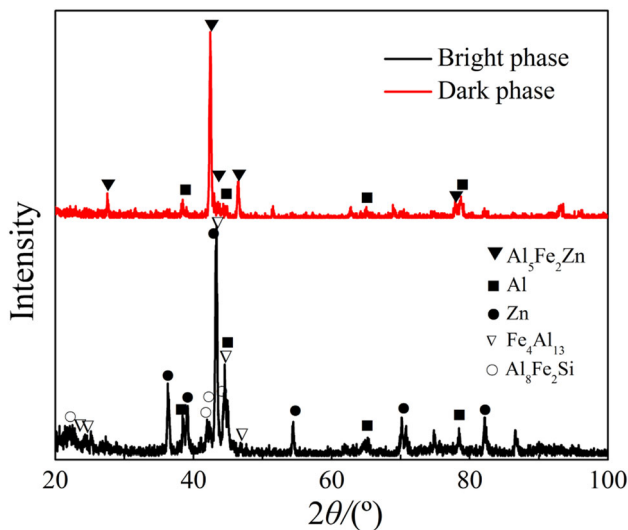

Fig. 9 XRD patterns of dark phase closest to steel substrate (red) and bright phase closest to Al–Zn metallic coating (black)
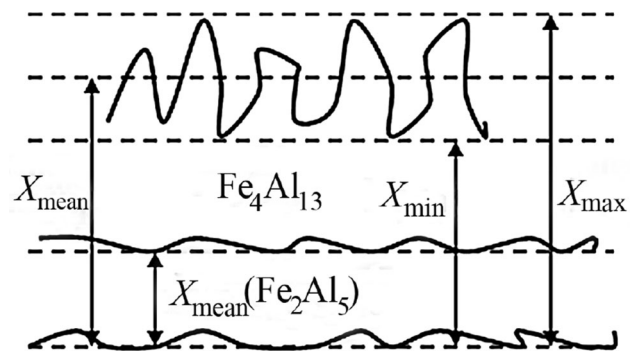

Fig. 10 Schematic showing thickness measurement of interfacial reaction layer [36]

would be very slow because of occupation by Mn restraining the growth of the interfacial reaction layer when Al or Fe atoms pass through the Fe–Al intermetallic compound. In this sample, the absence of oxygen is accounted for by the lack of an oxygen channel in the GDS, and it will be investigated in further experiments.

First-principle calculations were used to optimize the atomic structure, energy, and electronic structure of Mn-substituted Fe_2Al_5 phases to determine the effect of Mn on the growth of the interfacial reaction layer. In this study, the Vienna ab initio simulation package (VASP), which was developed at the University of Vienna by Kresse and Furthmüller [38], was employed. The generalized gradient
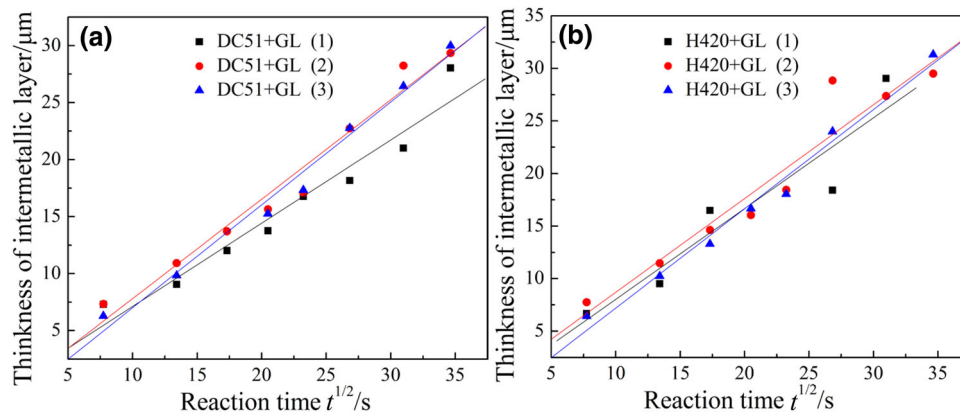
in DC51 + GL steel. In addition, the content of Mn in the interfacial reaction layer was correlated with the Mn content of the substrate. No new intermetallic compounds containing Mn were found based on thermodynamic calculations (Fig. 14) [31], and thus Mn may be present in a solid solution in the interfacial reaction layer. In that case, some Mn atoms would occupy vacancies in the orthorhombic Fe_2Al_5 structure. In addition, the growth rate

Fig. 11 Variation in interfacial reaction layer thickness with $t^{1/2}$ at 600 °C in DC51 + GL (**a**) and H420 + GL (**b**) steels from three parallel experiments

Table 4 Fitting parameters (see Fig. 11) related to interfacial reaction layer thicknesses in DC51 + GL and H420 + GL steels with respect to $t^{1/2}$

Material	Parameter	Value	Error	R^2
DC51 + GL (1)	k	0.73032	0.07071	0.93788
	c	− 0.18585	1.65446	
DC51 + GL (2)	k	0.87192	0.06424	0.96323
	c	− 0.91247	1.50321	
DC51 + GL (3)	k	0.90215	0.05105	0.98109
	c	− 2.01368	1.23242	
H420 + GL(1)	k	0.86286	0.17265	0.85703
	c	− 0.59654	3.63792	
H420 + GL(2)	k	0.89178	0.10524	0.91004
	c	− 0.21872	2.46241	
H420 + GL(3)	k	0.94355	0.05448	0.98033

R-Correlation coefficient

approximation (GGA) function of Perdew and Wang [39], along with the projector augmented wave (PAW) [40] method, was employed for all calculations to describe the exchange-correlation energy and the computationally expensive electron–ion interactions, respectively. A plane-wave basis set was used for the expansion of the single-particle Kohn–Sham wave functions. The sampling of the irreducible wedge of the Brillouin zone was performed with a regular Monkhorst–Pack grid of special k-points [41]. The ground-state atomic geometry was obtained by minimizing the Hellman–Feynman (H-F) forces using a conjugate gradient algorithm [42]. Atomic relaxation was achieved by using the calculated H-F forces as a guide in the process of adjusting the atomic configurations until the H-F force on each atom was less than 0.05 eV nm^{-1}. The calculations were performed on fast Fourier transform grids. The electronic structure of Fe_2Al_5 was first studied by constructing $(2 \times 1 \times 2)$ supercells consisting of 64 atoms (Fig. 15). The supercell of the $Fe_2(Al, Mn)_5$ phase was created to simulate Mn atom substitution at the Fe or Al atomic site. The corresponding kinetic energy cutoffs were 400 eV for all PAW calculations. For Brillouin zone integration, a $5 \times 5 \times 5$ Monkhorst–Pack grid of k-points was used for the calculation models.
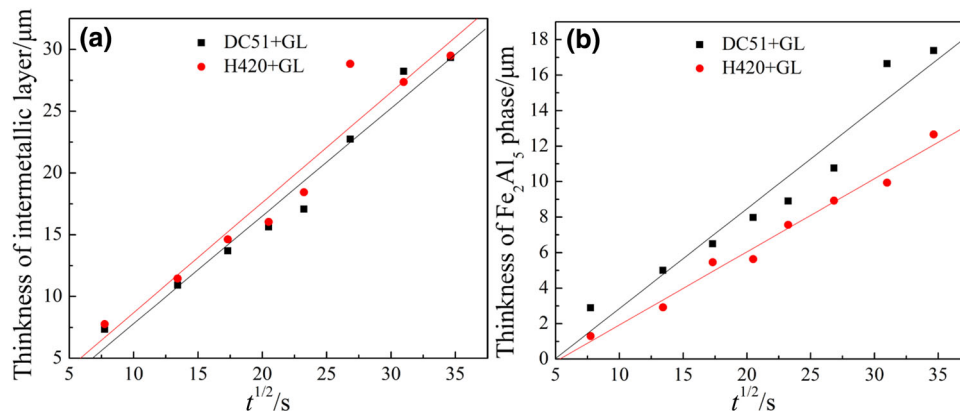

Fig. 12 Variation in total interfacial reaction layer thickness (**a**) and Fe_2Al_5 phase layer thickness (**b**) with $t^{1/2}$ for DC51 + GL and H420 + GL for an average of three parallel experiments at 600 °C

Table 5 Fitting parameters for variation in total interfacial reaction layer thickness and Fe$_2$Al$_5$ phase layer thickness (average of three parallel experiments) in DC51 + GL and H420 + GL with $t^{1/2}$

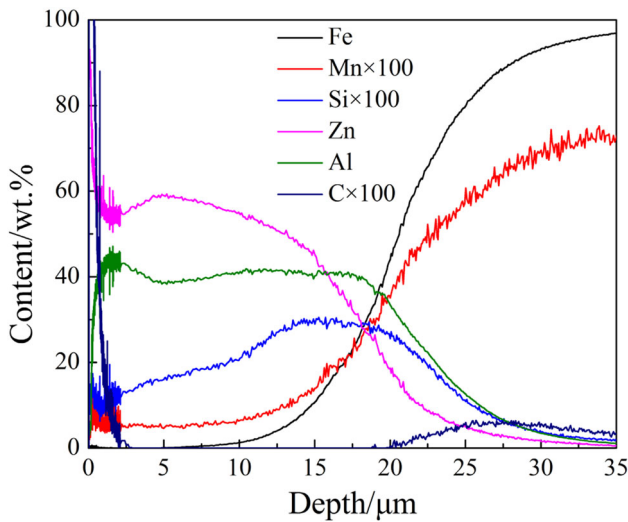| Layer	Material	Parameter	Value	Error	R^2
Total interfacial reaction layer	DC51 + GL	k	0.87192	0.06424	0.91004
		c	− 0.91247	1.50321	
	H420 + GL	k	0.89178	0.10524	0.96320
		c	− 0.21872	2.46241	
Fe$_2$Al$_5$ phase layer	DC51 + GL	k	0.56239	0.05774	0.97986
		c	− 2.77435	1.35104	
	H420 + GL	k	0.41188	0.02229	0.93060
		c	− 2.19427	0.52153	

Fig. 13 GDS curves of H420 surface coated with hot-dip galvalume for 180 s

The energies of Mn substitution at the Al and Fe sites were −323.372 and −318.816 eV, respectively. Thus, the energy of Mn substitution at Al sites is lower than that at Fe sites in the Fe$_2$Al$_5$ phase by 5.5 eV. This means that the most favorable sites for Mn substitution in the Fe$_2$Al$_5$
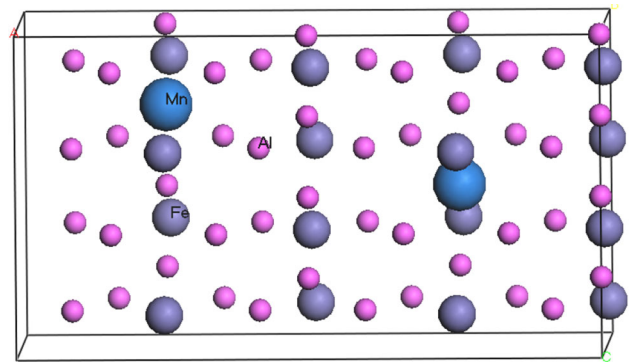

Fig. 15 Schematic of Mn substitution in bulk Fe$_2$Al$_5$. Large, medium, and small spheres corresponding to Mn, Fe, and Al, respectively

phase were Al atomic sites. Therefore, the bond energies and electronic structures of the Fe$_2$(Al, Mn)$_5$ supercell were calculated.

The bond energy difference (ΔE) between Mn and Al is defined by Eq. (1).

$$\Delta E = E_{Fe_2(Al,Mn)_5} - E_{Mn} - E_{Fe_2(Al,void)_5} \tag{1}$$

where $E_{Fe_2(Al,Mn)_5}$ is the total energy of the Fe$_2$(Al, Mn)$_5$ supercell structure; E_{Mn} is the energy of an Mn atom; and
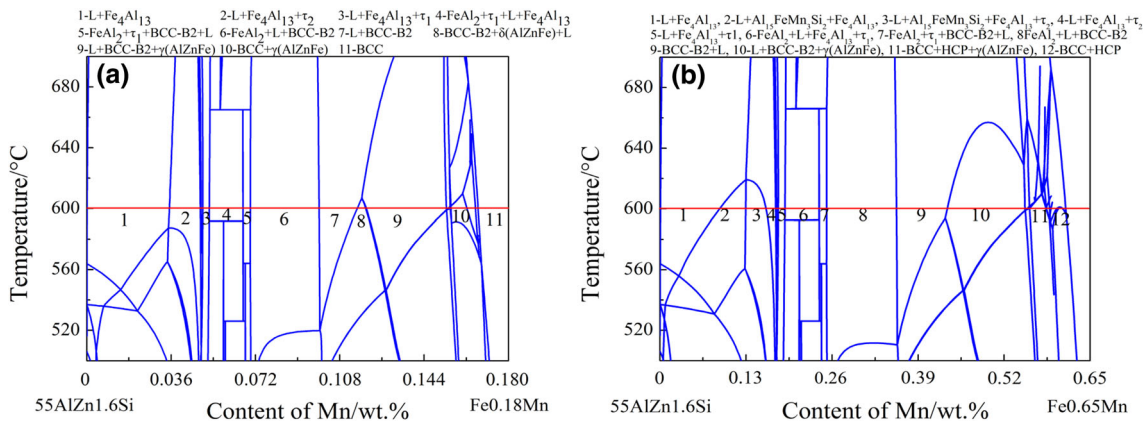

Fig. 14 Cross sections of Al–Zn–Si–Fe–Mn quinary diagrams. **a** 0–0.18 wt.% Mn; **b** 0–0.65 wt.% Mn
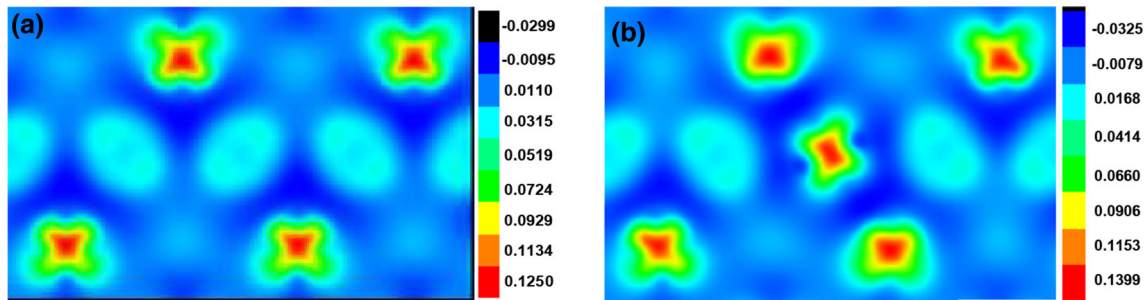
Fig. 16 Charge transfer profiles of pure Fe_2Al_5 (**a**) and Fe_2Al_5 with Mn substitution (**b**) on (400) plane

$E_{Fe_2(Al,void)_5}$ is the total energy of corresponding Fe_2Al_5 structure in which one Al atom was removed. Negative bond energies indicate greater stability compared to the corresponding void structure and Mn-substituted structure within this definition.

The calculated bond energies between Fe–Al and Mn–Al were −0.824 and −9.008 eV, respectively. The results show that the bonding energy between the Mn and Al atoms was stronger than the bonding energy between Fe and Al atoms. This means that the additional Mn atom may effectively prevent the formation of metallic bonds between Al and Fe, thereby inhibiting the growth of the Fe–Al phase.

In addition, the charge transfer on Mn substitution was calculated and is shown in Fig. 16, and the net electronic charges of Al and Fe in pure Fe_2Al_5 were 0.810 and 7.417 eV, respectively. The net electronic charges of Al, Fe, and Mn in Mn-sub Fe_2Al_5 were 0.812, 7.411, and 6.000 eV, respectively. It was found that the net electronic charge of the Fe atom decreased by about 0.013 and 0.026 eV in the Fe_2Al_5 and $FeAl_3$ systems, respectively, after Mn atoms were added, as shown in Fig. 16. Meanwhile, the net electronic charges of the Al atoms showed almost no change, but the net electronic charges of the Mn atoms were very high. This result indicated that the electronic charge of the Al atoms was transferred to the Mn atoms to a greater extent than to Fe atoms. Electronic charge transfer is a characteristic of bonding between effective additives and the matrix [43, 44]. Therefore, it could be deduced that the additional Mn atoms remove more electric charge from the Al atoms, even resulting in the formation of Mn–Al bonds and, eventually, reducing the thickness of the interfacial reaction layer.

4 Conclusions

1. The interfacial reaction layers of H420 + GL and DC51 + GL are mainly composed of the Fe_2Al_5 phase, which is closest to the steel substrate, an Fe_4Al_{13} phase, and Al_8Fe_2Si intermetallic compounds, which are closest to the metallic Al–Zn coating.

2. A carbon buildup exists ahead of the interface layer of H420 + GL, and this becomes more obvious with increasing reaction time. The reason for this is that the H420 steel contains more carbides than DC51 steel, and this cannot diffuse through the intermetallic layer during the interfacial reaction. The aluminum atoms drive out carbon atoms when they diffuse toward the interface, resulting in a carbon buildup ahead of the interface layer.

3. The thicknesses of the interfacial reaction layers in H420 + GL and DC51 + GL are almost the same, but the Fe_2Al_5 layer in H420 + GL is relatively thin when prepared under the same conditions as DC51 + GL. This indicates that the growth rate of the Fe_2Al_5 phase in high-strength low-alloy steel is lower than that in mild carbon steel.

4. A study of the electric charge shows that electronic charge was transferred more significantly from Al to Mn than Fe. Thus, the Mn atoms will remove more electric charge from the Al atoms, allowing the formation of Mn–Al bonds, which eventually results in a reduction in the thickness of the interfacial reaction layer.

References

[1] B.J. Xu, Nucleation and growth of 55% Al–Zn alloy on steel substrate, University of Wollongong, Wollongong, Australia, 2005.

[2] N. Takata, M. Nishimoto, S. Kobayashi, M. Takeyama, Intermetallics 67 (2015) 1–11.

[3] H. Shahverdi, M. Ghomashchi, S. Shabestari, J. Hejazi, J. Mater. Process. Tech. 124 (2002) 345–352.

[4] Y. Han, C. Ban, Q. Ba, S.J. Guo, S.H. Wang, J.Z. Cui, Mater. Lett. 60 (2006) 1884–1887.

[5] A. Bouayad, C. Gerometta, A. Belkebir, A. Ambari, Mater. Sci. Eng. A 363 (2003) 53–61.

[6] K.A. Nazari, S.G. Shabestari, J. Alloy. Compd. 478 (2009) 523–530.

[7] W.J. Cheng, C.J. Wang, Mater. Charact. 61 (2010) 467–473.

[8] H. Springer, A. Kostka, E.J. Payton, D. Raabe, A. Kaysser-Pyzalla, G. Eggeler, Acta Mater. 59 (2011) 1586–1600.

[9] W.M. Jiang, Z.T. Fan, G.Y. Li, L. Chi, J. Alloy. Compd. 678 (2016) 249–257.

[10] W.M. Jiang, Z.T. Fan, G.Y. Li, X.W. Liu, F.C. Liu, J. Alloy. Compd. 688 (2016) 742–751.

[11] D. Phelan, B.J. Xu, R. Dippenar, Mater. Sci. Eng. A 420 (2006) 144–149.

[12] H.P. Peng, X.P. Su, Z. Li, J.H. Wang, C.J. Wu, H. Tu, X.F. Lai, Surf. Coat. Technol. 206 (2012) 4329–4334.

[13] J.H. Selverian, A.R. Marder, M.R. Notis, Metall. Trans. A 19 (1988) 1193–1203.

[14] T.N. Vu, P. Volovitch, K. Ogle, Corros. Sci. 67 (2013) 42–49.

[15] G.X. Wu, J.Y. Zhang, Y.L. Ren, G.Y. Li, X.C. Wu, Q. Li, K.C. Chou, Metall. Mater. Trans. A 43 (2012) 2012–2017.

[16] G.X. Wu, J.Y. Zhang, Q. Li, K.C. Chou, X.C. Wu, Metall. Mater. Trans. B 43 (2012) 198–205.

[17] J. Lee, J. Park, S.H. Jeon, Metall. Mater. Trans. B 42 (2011) 1086–1089.

[18] M. Blumenau, M. Norden, F. Friedel, K. Peters, Surf. Coat. Technol. 205 (2011) 3319–3327.

[19] E.M. Bellhouse, A. Mertens, J.R. McDermid, Mater. Sci. Eng. A 463 (2007) 147–156.

[20] Z. Li, Research on the silicon reactivity and the influence of alloy elements on the hot-dip galvanizing, Central South University, Changsha, China, 2008.

[21] S. Shimada, Y. Takada, J. Lee, T. Tanaka, ISIJ Int. 48 (2008) 1246–1250.

[22] Y. Takada, S. Shimada, J. Lee, M. Kurosaki, T. Tanaka, ISIJ Int. 49 (2009) 100–104.

[23] X.S. Li, S.I. Baek, C.S. Oh, S.J. Kim, Y.M. Kim, Scripta Mater. 57 (2007) 113–116.

[24] A. Ollivier-Leduc, M.L. Giorgi, D. Balloy, J.B. Guillot, Corros. Sci. 52 (2010) 2498–2504.

[25] I. Cvijović, I. Parezanović, M. Spiegel, Corros. Sci. 48 (2006) 980–993.

[26] D.J. Willis, F. Ilinca, F. Ajersch, N. Setargew, Prog. Comput. Fluid. Dyn. 7 (2007) 183–194.

[27] J. Strutzenberger, J. Faderl, Metall. Mater. Trans. A 29 (1998) 631–646.

[28] S.H. Hwang, J.H. Song, Y.S. Kim, Mater. Sci. Eng. A 390 (2005) 437–443.

[29] J.H. Selverian, M.R. Notis, A.R. Marder, J. Mater. Eng. 9 (1987) 133–140.

[30] W.S. Cao, S.L. Chen, F. Zhang, K. Wu, Y. Yang, Y.A. Chang, R. Schmin-Fetzer, W.A. Oates, Calphad 33 (2009) 328–342.

[31] PanAl-Aluminium Alloy Thermodynamic Database, in: CompuTherm, Madison, WI, USA, 2015.

[32] B.J. Xu, D. Phelan, R. Dippenaar, Mater. Sci. Eng. A 473 (2008) 76–80.

[33] G.H. Awan, F. Ul Hasan, Mater. Sci. Eng. A 472 (2008) 157-165.

[34] M. Yousaf, J. Iqbal, M. Ajmal, Mater. Charact. 62 (2011) 517–525.

[35] T. Sasaki, T. Yakou, K. Mochiduki, K. Ichinose, ISIJ Int. 45 (2005) 1887–1892.

[36] K. Bouche, F. Barbier, A. Coulet, Mater. Sci. Eng. A 249 (1998) 167–175.

[37] R. Richards, R. Jones, P. Clements, H. Clarke, Int. Mater. Rev. 39 (1994) 191–212.

[38] G. Kresse, J. Furthmüller, Phys. Rev. B 54 (1996) 11169–11186.

[39] J.P. Perdew, J. Chevary, S.H. Vosko, K.A. Jackson, M.R. Pederson, D.J. Singh, C. Fiolhais, Phys. Rev. B 46 (1992) 6671–6687.

[40] P.E. Blöchl, Phys. Rev. B 50 (1994) 17953–17979.

[41] H.J. Monkhorst, J.D. Pack, Phys. Rev. B 13 (1976) 5188–5192.

[42] M.P. Levin, in Numerical Recipes in Fortran 90: the art of parallel scientific computing, E-Publishing: IEEE Computer Society, New York, USA, 1998, pp. 79.

[43] H.M. Jin, Y. Li, H.L. Liu, P. Wu, Chem. Mater. 12 (2000) 1879–1883.

[44] P. Wu, H.M. Jin, H.L. Liu, Chem. Mater. 14 (2002) 832–837.